Homogeneous CoO on Graphene for Binder-Free and Ultralong-Life Lithium Ion Batteries

Xiao-lei Huang, Ru-zhi Wang, Dan Xu, Zhong-li Wang, Heng-guo Wang, Ji-jing Xu, Zhong Wu, Qing-chao Liu, Yu Zhang, and Xin-bo Zhang**

Ultralong cycle life, high energy, and power density rechargeable lithium-ion batteries are crucial to the ever-increasing large-scale electric energy storage for renewable energy and sustainable road transport. However, the commercial graphite anode cannot perform this challenging task due to its low theoretical capacity and poor rate-capability performance. Metal oxides hold much higher capacity but still are plagued by low rate capability and serious capacity degradation. Here, a novel strategy is developed to prepare binder-free and mechanically robust CoO/graphene electrodes, wherein homogenous and full coating of β-$Co(OH)_2$ nanosheets on graphene, through a novel electrostatic induced spread growth method, plays a key role. The combined advantages of large 2D surface and moderate inflexibility of the as-obtained β-$Co(OH)_2$/graphene hybrid enables its easy coating on Cu foil by a simple layer-by-layer stacking process. Devices made with these electrodes exhibit high rate capability over a temperature range from 0 to 55 °C and, most importantly, maintain excellent cycle stability up to 5000 cycles even at a high current density.

1. Introduction

The ever-growing demand for large-scale energy storage applications in electric vehicles and renewable energy systems has spurred significant research efforts on long cycle life, high-capacity, and high power lithium-ion batteries (LIBs).[1] The commercial graphite anode can not meet these challenges due to its low theoretical capacity.[2] There is a consensus that the breakthrough in capacity could be achieved by moving from classical intercalation reaction to conversion reaction.[2b,3] However, even after a decade of intensive efforts, the formidable capacity degradation and poor rate performance still seriously hamper the practical application of conversion-based materials in LIBs.

On the other hand, in a traditional electrode, polymeric binder plays an essential role to integrate individual electroactive particles. Although intensive research has been focused on synthesis of high performance electroactive materials, less attention is devoted to the advancement of binder. However, recently the widely used organic binder (polyvinylidene fluoride, PVDF) is found to swell easily in common electrolyte with EC/DMC solvent, leading to seriously poor stability and irreversible capacity losses.[4] This is adding insult to injury for electrodes where severe expansion/shrinkage during the lithiation/delithiation process already exist. Although cycling degradation has been alleviated by employing superior polymeric binders,[4,5] it does not provide a single "silver bullet". Furthermore, adding of inactive and insulate polymeric binders would inevitably impede the efforts to improve the capacity, rate capability, and decrease the manufacturing costs of LIBs, which is of critical importance to large-scale electric energy storage applications. Alternatively, binder-free electrodes have been fabricated on current collectors through various methods such as chemical vapor deposition,[6] electrodeposition,[7] and hydrothermal synthesis,[8] all these methods suffer from more or less severe drawbacks like requirement of special equipment, complication of preparation process, energy and time-consuming, and impossibility of large scale fabrication with low-cost. Therefore, developing a new strategy to fabrication high-performance binder-free electrode is urgently desirable and of great importance.

Transition-metal oxides (TMOs) are proposed as promising anode materials due to their abundance, low cost, and high theoretical capacity. Unfortunately, like other conversion-based anode materials, their practical application in LIBs is still hindered by its poor cycle stability and rate capability due to their low conductivity and drastic volume variation during the lithium uptake and release process.[9] To meet these challenges, downsizing theTMOs to nanoscale and constructing hybrid materials

X.-l. Huang, Dr. D. Xu, Dr. Z.-l. Wang, Dr. H.-G. Wang, Dr. J.-J. Xu, Z. Wu, Q.-C. Liu, Prof. X.-B. Zhang
State Key Laboratory of Rare Earth Resource Utilization
Changchun Institute of Applied Chemistry
Chinese Academy of Sciences
Changchun, 130022 P. R. China
E-mail: xbzhang@ciac.jl.cn

X.-l. Huang, Z. Wu
University of Chinese Academy of Sciences
Beijing, 100049 P. R. China

Prof. R.-Z. Wang
College of Materials Science and Engineering
Beijing University of Technology
Beijing, 100124 P. R. China

Prof. Y. Zhang
School of Chemistry and Environment
Beihang University
Beijing, 100191 P. R. China
E-mail: jade@buaa.edu.cn

DOI: 10.1002/adfm.201203777

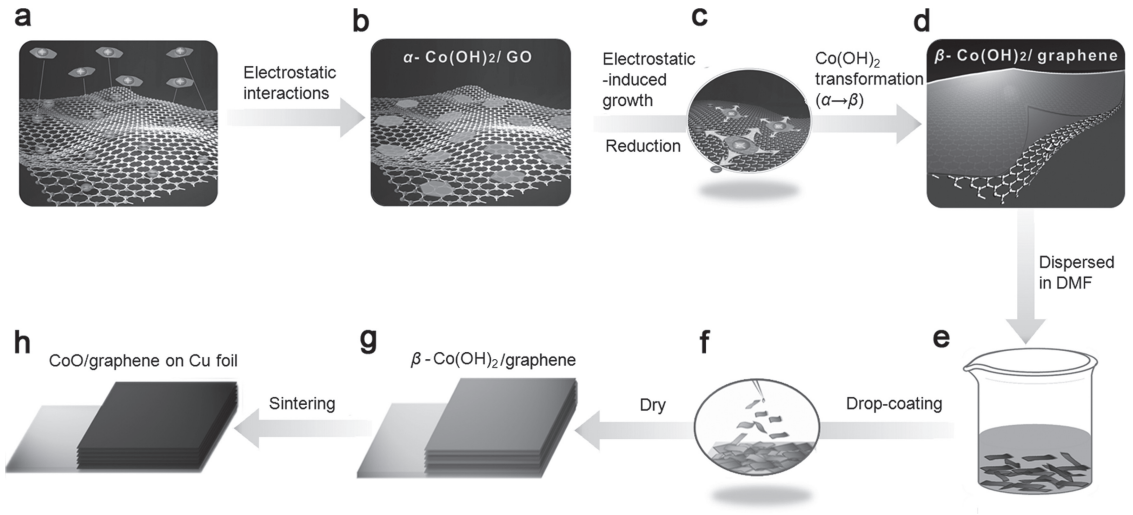

Figure 1. a) Schematic diagram of graphene oxide with negative charge and α-$Co(OH)_2$ with positive charge. b) Electrostatic interactions of graphene oxide and α-$Co(OH)_2$. c) Growth process of electrostatic-induced spread growth method. d) Homogeneous β-$Co(OH)_2$ on graphene. e) β-$Co(OH)_2$/graphene hybrid dispersed in N,N-dimethyl formamide (DMF). f) The process of drop-coated method. g) β-$Co(OH)_2$/graphene hybrid on Cu foil. h) CoO/graphene hybrid on Cu foil.

with highly electrical conductive, flexible, and chemically stable graphene have been proposed to be one of the most promising strategies. However, TMO nanoparticles (NPs) aggregation-derived degradation in capacity still exists because the contact between graphene and the TMO NPs is not tight enough.[10]

To meet these challenges, presumably, TMOs in large area nanosheets (NSs) structure could intrinsically facilitate stable assembly with graphene and then easy coating on Cu foil, enabling a binder-free electrode. Consequently, the advantageous combination of the greatly alleviated aggregation of TMOs NPs and volume variation, derived from the intrinsically high immobility and facile strain relaxation of large area NSs structure, and absence of binder swelling, would theoretically enhance the structural stability and thus the cycle performance. Even more important, the large area of highly conducting graphene and absence of non-conducting polymeric binder could offers high lithium ion flux, continuous and fast conducting pathways for electrons throughout the electrodes, which would benefit the power and energy density. However, if this alluring promise is to turn into reality, ensurance of uniform, full and tight coating of TMOs NSs on graphene is prerequisite. To the best of our knowledge, compared to work on assembly of 0D spherical TMOs NPs with graphene,[10,11] homogenous coating of TMOs NSs on graphene toward a high-performance binder-free electrode is highly desirable but still very challenging.

Here, as a proof-of-concept experiment, we demonstrate an effective electrostatic induced spread growth method to homogeneously and completely coat β-$Co(OH)_2$ NSs on graphene, which enables its easy and firm coating on Cu foil toward a binder-free CoO/graphene electrode. When employed as anode in LIBs, high capacity and cycling stability over a temperature range from 0 to 55 °C, good rate capability of 172 mA h g^{-1} even at a high current density of 20 A g^{-1}, and especially, excellent cycle stability even after 5000 cycles at 1 A g^{-1} are successfully obtained, which is far exceeds the best reported for conversation reaction of metal oxides.[5,12]

2. Results and Discussion

Figure 1 shows the schematic illustration of the synthesis strategy toward the binder-free CoO/graphene electrode, wherein the most critical point is to ensure homogeneous and complete coating of β-$Co(OH)_2$ NSs on graphene (Figure 1a–d), which is realized through a novel electrostatic induced spread growth method. In a typical synthesis, ultrathin α-$Co(OH)_2$ NSs with the thickness of ca. 2.6 nm are rapidly synthesized by a hydrothermal route (**Figure 2**a,b). All the strong diffraction peaks of the hybrid could be indexed to a hexagonal structure of α-$Co(OH)_2$ (Figure 2e),[13] and the graphene oxide (GO) is synthesized according to the modified Hummer's method starting from graphite powders. Importantly, the as-obtained α-$Co(OH)_2$ NSs are positively charged (ζ = +31.5 mV) while the graphene oxide is negatively charge (ζ = –68 mV) and thus composite can be well assembled driven by the mutual electrostatic interactions (Figure 1a,b and Supporting Information Figure S1). It is worth noting that, thanks to its high surface area of few-layer GO,[14] small amount of GO used could effectively adsorb a large number of ultrathin α-$Co(OH)_2$ NSs without compromising the capacity of the hybrid (vide infra). Finally, upon a reflux reaction in reductive condition, the α-$Co(OH)_2$ NSs are transformed into β-$Co(OH)_2$ (Figure 2 and **Figure 3**) and graphene oxide is reduced to graphene. The D/G intensity ratios (I_D/I_G) of Raman spectra is then used to check the reduction of graphene oxide.[15a] As shown in Figure S2a,b (Supporting Information), I_D/I_G changes from 0.84 to 1.05 after chemical reduction, indicating that oxygen-containing functional groups in graphene oxide is effectively removed and subsequently more defects are formed,[15] which is consistent with the XPS result (Supporting Information Figure S3). Unexpectedly, during the transformation process, the β-$Co(OH)_2$ grows, spreads, and finally fully and uniformly coats on graphene through the electrostatic induced spread growth method (Figure 1c, Supporting Information Figure S4). Namely, the

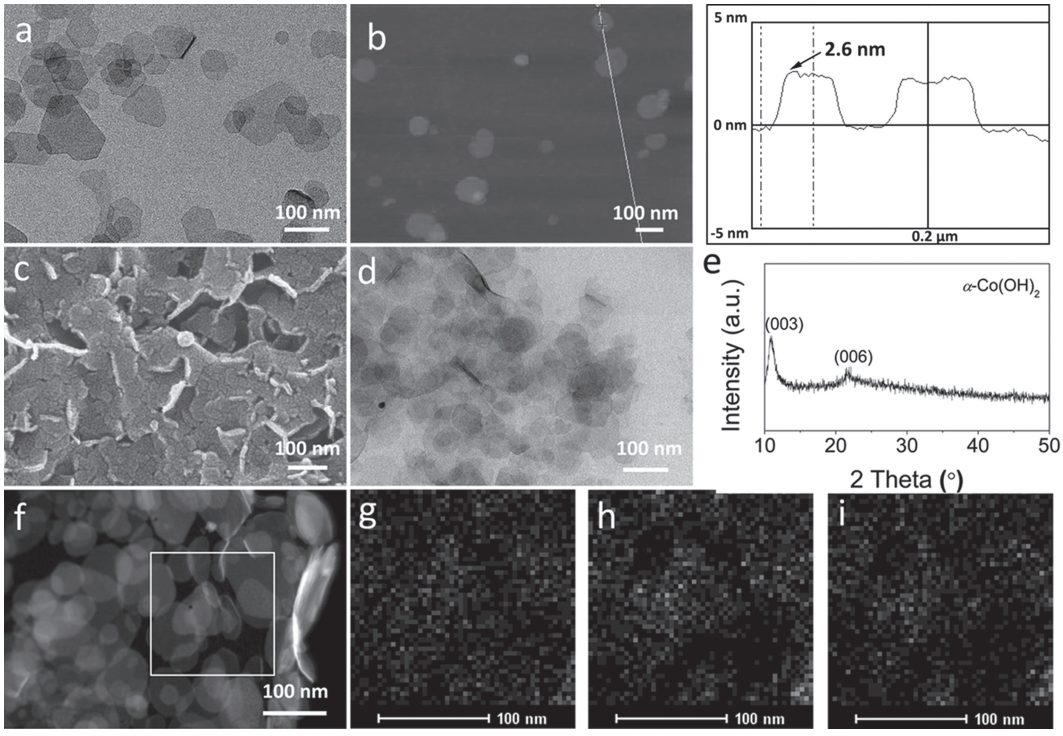

Figure 2. a) Low magnification TEM image and b) AFM image of α-$Co(OH)_2$. c) SEM image of α-$Co(OH)_2$/graphene oxide composite. d) TEM image of α-$Co(OH)_2$/graphene oxide composite. e) XRD pattern of α-$Co(OH)_2$/graphene oxide composite. f) Dark-field TEM image of α-$Co(OH)_2$/graphene oxide composite and corresponding elemental mapping images of g) carbon, h) cobalt, and i) oxygen in the selected area (white rectangle in (f)).

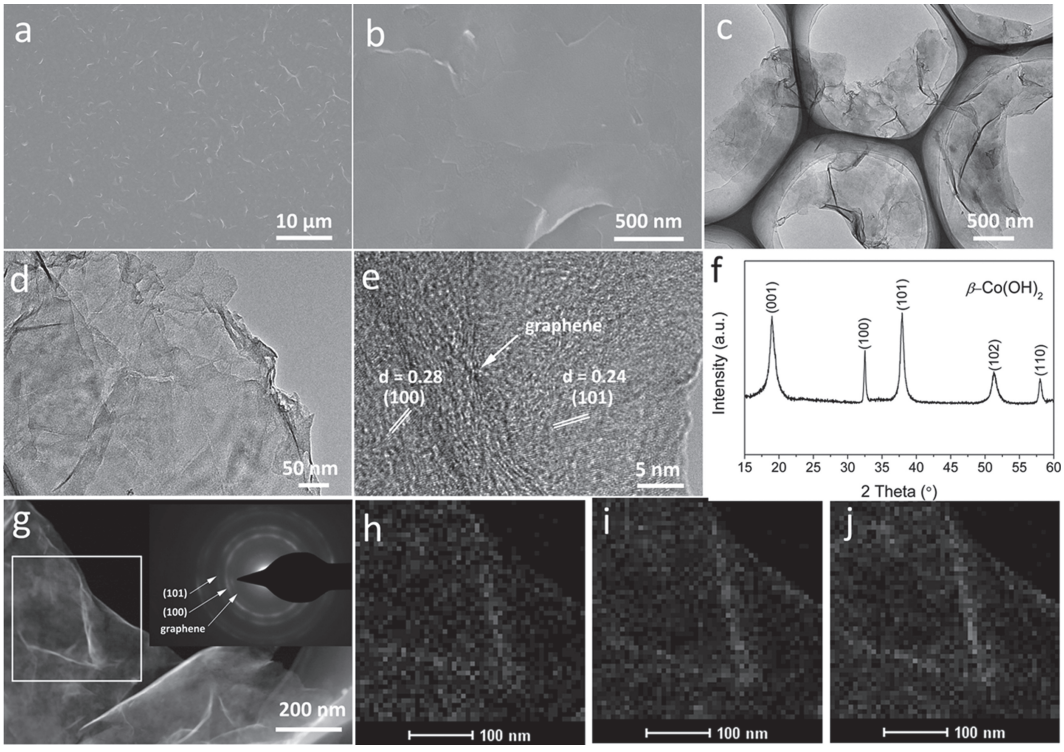

Figure 3. a) Low magnification and b) high magnification SEM images of β-$Co(OH)_2$/graphene hybrid on silicon wafer. c,d) Low magnification and e) high magnification TEM images of β-$Co(OH)_2$/graphene hybrid. f) XRD spectrum of β-$Co(OH)_2$/graphene hybrid. g) Dark-field TEM image and corresponding elemental mapping images of h) carbon, i) cobalt, and j) oxygen in the selected area (white rectangle in (g)). Inset in (g) shows the SAED pattern of β-$Co(OH)_2$/graphene hybrid.

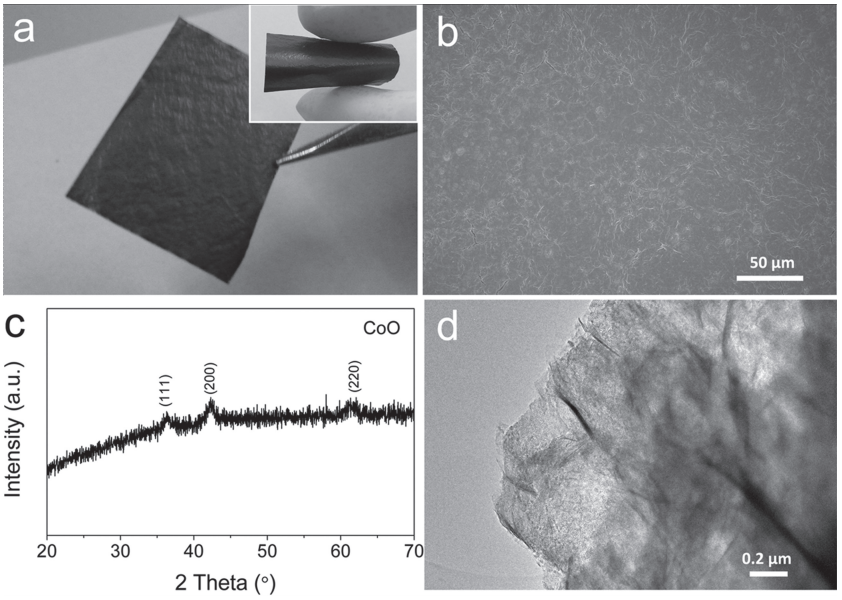

Figure 4. a) Photograph of CoO/graphene on Cu foil. Inset shows the bending deformation of binder-free electrode. b) SEM images of as-obtained electrode. c) XRD spectrum of CoO/graphene hybrid. d) TEM image of CoO/graphene hybrid.

mutual electrostatic adsorption, between positively charged α-$Co(OH)_2$ and β-$Co(OH)_2$ (ζ = +52.1 mV) and negatively charged graphene oxide and graphene (ζ = –14 mV), induces the growth along the graphene surface during the transformation process of $Co(OH)_2$ (α to β phase). The zeta potential measurements of all materials are in the same solvent used for materials synthesis (Supporting Information Figure S1). Figure 1e–h shows the fabrication process of the binder-free electrode. The above synthesized β-$Co(OH)_2$ NSs/graphene hybrid is firstly well dispersed in DMF, and then drop-coated on Cu foil. After sintering in reducing atmosphere, binder-free CoO/graphene electrode (**Figure 4**a) is successfully fabricated (the weight of active materials is ca. 0.53 mg cm^{-2}). The content of carbon in CoO/graphene hybrid is ≈13 wt%, as revealed by thermal-gravimetric measurements (Supporting Information Figure S5).

In order to demonstrate the homogeneous and full coating of β-$Co(OH)_2$ NSs on graphene, scanning electron microscopy (SEM) and transmission electron microscope (TEM) are employed. As shown in Figure 3a–c, β-$Co(OH)_2$/graphene hybrid possesses a larger-area sheet-like morphology, and can be easily stacked on flat silica wafer substrate. In addition, Figure 3d shows the as-obtained sheet-like β-$Co(OH)_2$/graphene hybrid is multi-layer. We may then assume that as-obtained β-$Co(OH)_2$ on graphene is ultrathin due to ultrathin α-$Co(OH)_2$. Furthermore, the distribution of graphene and β-$Co(OH)_2$ NSs in the hybrid is analyzed by energy dispersive X-ray (EDX) spectroscopy mapping technique (Figure 3g–j). The results clearly show that the elements of C, Co, O are distributed homogeneously, indicating that the coating of β-$Co(OH)_2$ on graphene is uniform and complete. More importantly, the thus obtained β-$Co(OH)_2$/graphene hybrid ensures it easily coated on Cu foil by layer-by-layer stacking process to form a homogenous, flat, and binder-free electrode (Supporting Information Figure S6a). On the contrary, only seriously aggregated, discontinuous, and incomplete coating can be obtained for α-$Co(OH)_2$/GO composite (Supporting Information Figure S6b), which might attribute that the coating of α-$Co(OH)_2$ on graphene oxide is quite inhomogeneous (Figure 2d,f–i) and thus lead to irregularly stacked together with a larger pore volume (Figure 2c). These results highlight the importance and power of our proposed electrostatic induced spread growth strategy to ensure homogenous, complete, and tight coating of graphene with ultrathin β-$Co(OH)_2$ NSs, with which the β-$Co(OH)_2$ NSs can effectively endow relative rigidity to flexible graphene and thus avoid aggregation during drop-coated process (Figure 3a,b).

After sintering, as shown in Figure 4a,b, no detachment of active materials from Cu foil is observed even after bending deformation. It should be note that layered structure (Figure 4d and Supporting Information Figure S8a) and good structural stability are still remained after the sintering process. In addition, Figure S7a (Supporting Information) shows layer-by-layer stacking of CoO/graphene hybrid, which further demonstrates the feasibility of our proposed strategy for preparation of binder-free electrode. On the other hand, the crystal structure of the obtained sample is characterized by X-ray diffraction (XRD) pattern (Figure 4c). All the diffraction peaks of sample can be indexed to a cubic structure of CoO (JCPDS card, No. 65-2902). These results indicate the successful synthesis of the CoO/graphene hybrid. On the contrary, without graphene, pure α-$Co(OH)_2$ can be transformed to relatively inactive metallic cobalt with small amount of CoO under the same condition due to unstable structure (Supporting Information Figure S9). After sintering under reducing atmosphere, it can be found that the G bands in the Raman spectrum of CoO/graphene hybrid exhibit obvious blue shifts (Supporting Information Figure S2c) compared with β-$Co(OH)_2$/graphene hybrid (Supporting Information Figure S2b) and chemical reduced graphene (Supporting Information Figure S2d), indicating that the presence of

a charge transfer from graphene to CoO and carbon atoms in graphene attached to oxygen in CoO.[3b] The I_D/I_G of CoO/graphene hybrid is found to be 1.03, indicating more defect formed accompanying with the further reduction of graphene oxide during sintering. Figure S8a (Supporting Information) depicts the corresponding selected area electron-diffraction (SAED) pattern of the CoO/graphene hybrid. There is two set of diffraction patterns that belong to the cubic CoO and graphene. Note that the weak diffraction ring from graphene is obvious due to multilayer graphene. Figure S7b (Supporting Information) shows a representative high resolution TEM image of the CoO/graphene hybrid. The marked interplanar d spacing of 0.21 and 0.25 nm correspond to those of the (111) and (200) lattice planes of the cubic CoO, respectively, further confirming the CoO coating on graphene. In addition, the SAED pattern showing diffraction ring from graphene can also be found in Supporting Information Figure S7b. Furthermore, EDX scanning elements mapping (Figure S8c–f) of Co, O, and C is employed to obtain the spatial distributions of the atomic contents across the CoO/graphene hybrid. A homogeneous coexistence of the three elements directly features the homogenous and complete coating of CoO on graphene in the obtained binder-free electrode. In addition, the as-obtained CoO on graphene should be ultrathin due to ultrathin $Co(OH)_2$ precursor. This unique configuration is expected to achieve a high performance, which will be discussed in detail in the following. It should be noted that a large number of mesopores generated in hybrid after sintering (Supporting Information Figure S8a). The Barrett-Joyner-Halenda analysis (Supporting Information Figure S8b) shows that as-obtained mesopores are about 2–6 nm in size, which might be due to the structure reconstruction and/or onward diffusion of the released of water vapor on the surface of graphene. In addition, there are some larger pores with the size of 10–140 nm, owing to the void space of between the layers and layers. These pores could offer sufficient contact interface between TMOs and electrolyte, and thus ensure higher utilization rate of TMOs especially at higher current density.

Coin cells with metallic Li counter electrode are assembled and galvanostatic charge/discharge technique is employed to evaluate the electrochemical performance of binder-free CoO/graphene electrode. **Figure 5**a shows the charge/discharge voltage profiles cycled under a current density of 100 mA g^{-1} in the voltage range of 0.01–3.0 V vs. Li/Li^+. The initial discharge and charge specific capacities are 947 and 678 mA h g^{-1}, respectively, based on the whole weight of the hybrid. The large initial discharge capacity of the CoO/graphene hybrid could be mainly attributed to the formation of the solid electrolyte interface (SEI) film on the surface of the electrode due to the electrolyte decomposition,[16] in accordance with the cyclic voltammograms analysis in Supporting Information Figure S10. It should be pointed out that the reversibility of capacity is significantly improved with an average columbic efficiency of >97% from the second cycle, indicating that the formed SEI during the first cycle is favorable and stable. Impressively, as shown in Figure 5b, when cycled at low current density of 100 mA g^{-1}, the anode retains its capacity very well for 150 full charge/discharge cycles. The capacity of the 150th cycle is still as high as 640 mA h g^{-1}, which is 89.6% of that theoretical capacity of CoO (714 mA h g^{-1}).

To further evaluate the cycle stability of binder-free electrode, we test the charge/discharge performance at a much higher current density of 1 A g^{-1}. Surprisingly, as shown in Figure 5c (black), the electrode retains its capacity very well for 5000 full charge/discharge cycles. The capacity of the 5000th cycle is still as high as 604 mA h g^{-1}. Meanwhile, the coulombic efficiency is very close to 100% all over the 5000 cycles after 1 cycle (Figure 5c). For comparison, the cycling performance of CoO/graphene electrode with PVDF binder is also estimated at the same condition. As shown in Figure 5c (light grey), the capacity of electrode decreases from 546 to only 256 mA h g^{-1} only after 1000 cycles, indicating very poor cycling stability. The voltage-capacity profiles of electrode are also shown in Figure 5d,e. The potential shows a sloping profile within a cutoff window of 0.01–3.0 V after 1 cycle, which is consistent with the behavior of conversion reaction of TMOs.[8,16b] No larger capacity change in Figure 5d can be found even after 5000 cycles, showing excellent cycling stability of as-prepared binder-free electrode. This result demonstrates an significant improvement in cycling life compared with other improved methods of previous reports (600 cycles at low current density).[5,12b] The obtained excellent cycle stability of the binder-free CoO/graphene electrode reflects synergy of the sample's three unique characteristics: 1) Pulverization of active material during cycling has been considered to be a main reason for poor cycling stability.[17] In our work, the homogeneous and complete combination of ultrathin mesopore CoO with elastic graphene can effectively alleviate the aggregation and the physical strains, ensuring less pulverization and exfoliation from current collector. It should be point that mesopore CoO and 2D flake structure can efficiently buffer volume changes as shown in **Figure 6** as discussed below. 2) The CoO coated on sheet-like graphene with appropriate pore volume (Supporting Information Figure S8b) can lead to the formation of paths for lithium ion transport between the electrolyte and active material and buffer volume changes during cycling. In addition, graphene exhibit excellent electronic conductivity, insulating Li_2O form on graphene due to CoO on graphene during discharge process. Thus this hybrid can alleviate polarization during charge and discharge. 3) The free of binder can essentially surmount the problem of the swelling-induced cycling degradation.[4,18] To confirm the structure stability of the CoO/graphene hybrid upon cycle, we investigate the morphology of CoO/graphene hybrid after 1000 charge/discharge cycles. As shown in Figure 6a, the sheet-like morphology of the CoO/graphene hybrid and the homogeneous distribution of the elements of C, Co, and O still remain (Figure 6b–e). In addition, after the cycling test, the voltage profile also kept unchanged (Figure 5d). These results indicate that the as-prepared CoO/graphene hybrid and binder-free electrode are very stable during the required lifetime of commercial LIBs.

Another outstanding performance is the rate capability of the binder-free CoO/graphene electrode compared with that with PVDF. Figure 5f demonstrates the rate capability of the two electrodes from current densities of 0.5 to 20 A g^{-1}. At moderate current densities (0.5 and 1 A g^{-1}), the capacities of electrode with PVDF are ≈620 and 560 mA h g^{-1}, respectively. This good performance could be attributed to the unique properties of the CoO/graphene hybrid. However, the binder-free CoO/graphene electrode shows much higher capacity than

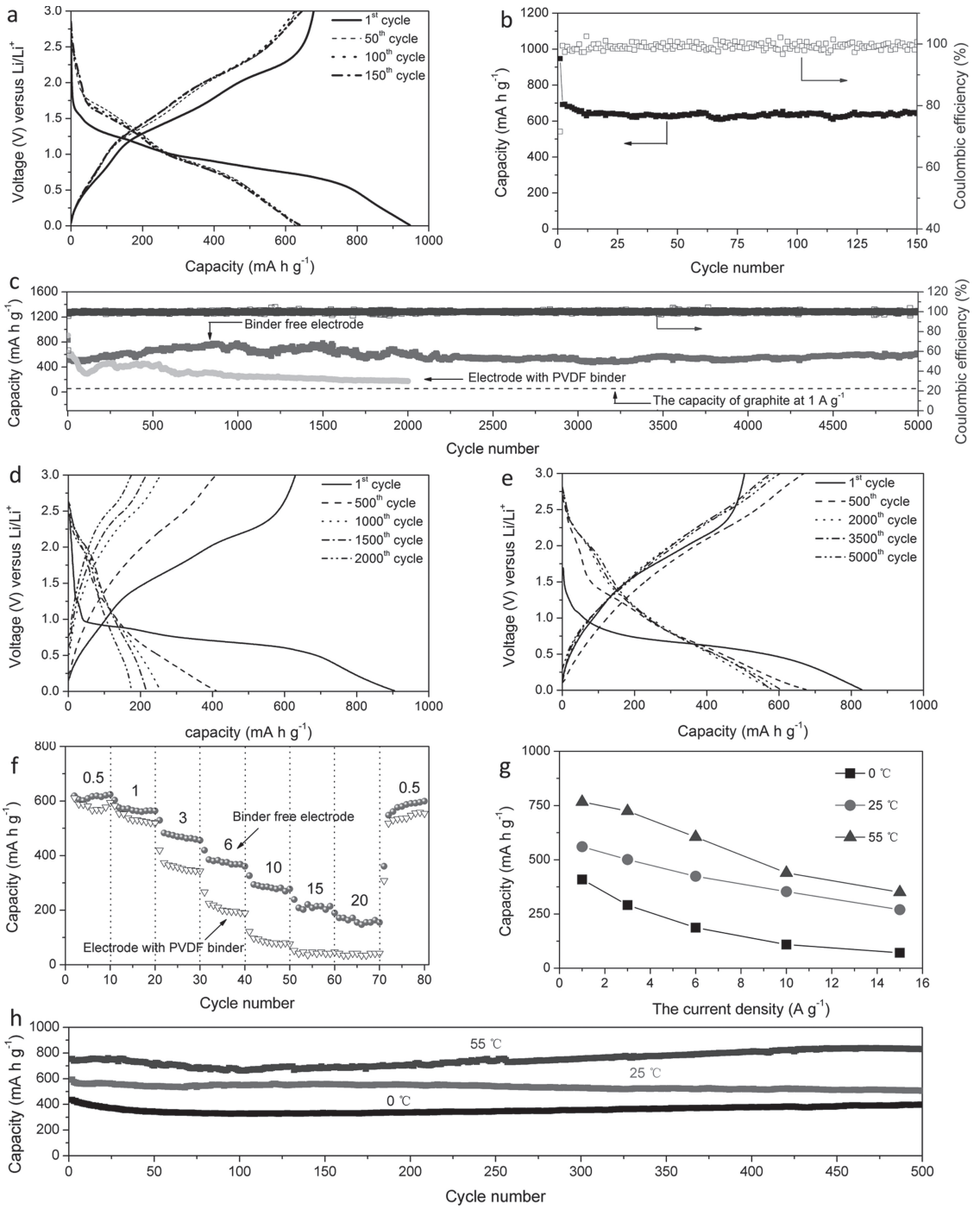

Figure 5. a) Galvanostatic discharge/charge profiles and b) reversible Li extraction capacity of binder-free electrode of at 0.1 A g^{-1}. c) Reversible Li extraction capacity of CoO/graphene hybrid electrode at 1 A g^{-1} for 5000 cycles. d) Galvanostatic discharge/charge profiles of binder-free electrode and e) electrode with PVDF binder at 1 A g^{-1}. f) Rate-capability performance of binder-free electrode and electrode with PVDF binder after the first charge/discharge cycle. The number on image indicated the current density (A g^{-1}). The discharge current density equaled to the charge current density at discharge/charge process. g) Rate-capability performance of binder-free electrode at 0, 25 and 55 °C. The cells were performed at the charge current density of 1 A g^{-1}. h) Reversible Li extraction capacity of binder-free electrode at 1 A g^{-1} from 0 to 55 °C after the first discharge/charge cycle. All electrochemical measurements (a–f) were performed at room temperature in two-electrode 2025 coin-type half-cells cycled between 0.01 V and 3 V.

that with PVDF binder under all investigated current densities higher than 1 A g^{-1}. For example, at the current density of 6 A g^{-1}, the binder-free CoO/graphene electrode still exhibits a favorable specific capacity of 385 mA h g^{-1} after 30 cycles, which is still higher than the theoretical capacity of graphite, while the electrode with PVDF shows a specific capacity of

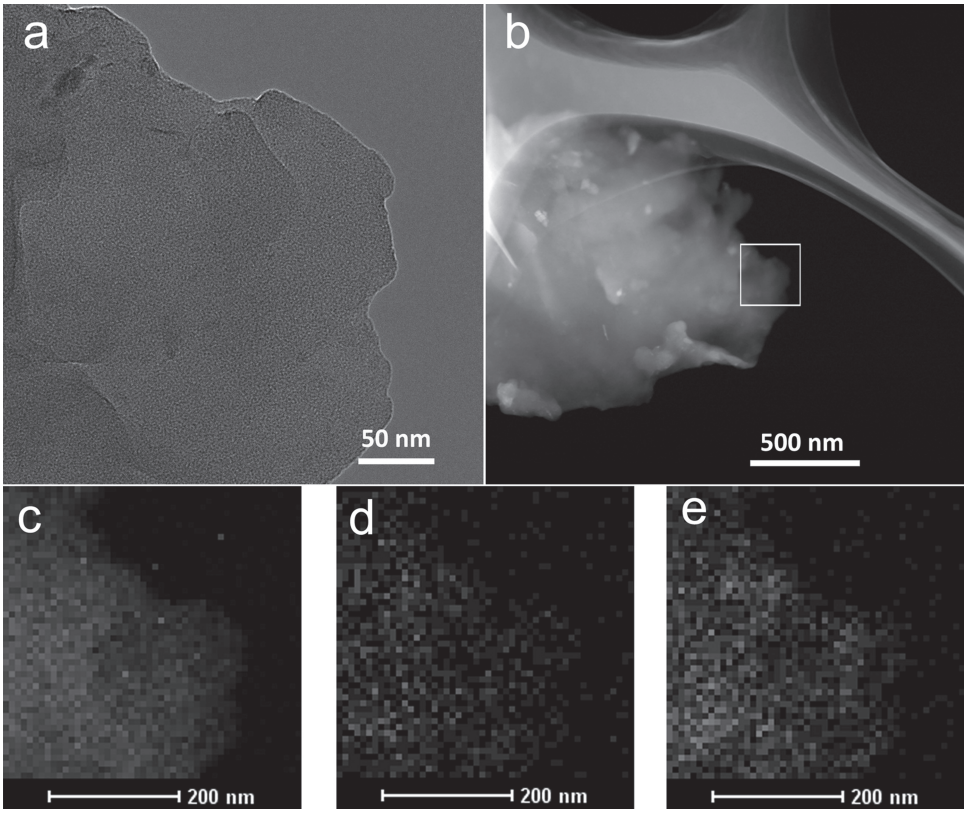

Figure 6. a) TEM image of CoO/graphene hybrid after 1000 charge/discharge cycles at 1 A g^{-1}. b) TEM image and corresponding elemental mapping images of c) carbon, d) cobalt, and e) oxygen in the selected area (white rectangle in (b)).

224 mA h g^{-1}. Unexpectedly, at a very high current density of 20 A g^{-1}, binder-free electrode is still able to deliver discharge capacity of ≈170 mA h g^{-1}, which is much higher than these of electrode with PVDF binder (only ≈40 mA h g^{-1}). Importantly, after the high rate measurements, the specific capacities of the two types of electrode cycled under 0.5 A g^{-1} are able to recover to the initial reversible values, implying the stable structure of CoO/graphene hybrid and their good reversibility.

The results above undoubtedly demonstrate the high rate performance of binder-free ultrathin CoO/graphene electrode. As a previous study shows, for LIBs to achieve a high power density, rapid lithium ionic and electronic diffusion in electrode materials are necessary. In our case, the CoO is very thin and thus could shorten the lithium ion and electron diffusion time. The intimate contact of CoO NSs with highly conductive graphene could guarantee fast and continuous electron transport. Meanwhile, the absence of non-conducting PVDF binder could also improve the electrode electronic conductivity. These unique characteristics lead to the competitive advantages of the ultrathin CoO NSs/graphene-based LIB anode.

When a battery delivers high power, the temperature can increase significantly due to the Joule effect. Therefore, it is crucial to study the temperature-dependent performance to evaluate feasibility for real application. Measurements are carried out at 0, 25, and 55 °C. Figure 5g clearly shows that the increasing temperature improves rate-capability of electrode because the ion mobility in the electrolyte and active material can be enhanced.[19] Furthermore, Figure 5h shows binder-free electrode exhibits excellent cycling stability over a wide temperature range from 0 to 55 °C. Importantly, when cycling at low temperature of 0 °C, the electrode still exhibits a high capacity of 320–430 mA h g^{-1} at 1 A g^{-1}. After 500 cycles, the capacity is ≈390 mA h g^{-1}. This result shows as-obtained electrode is to the benefit of the batteries worked at low temperature. At higher temperature (55 °C), the cycling stability still remains at the current density of 1 A g^{-1}. The capacity of electrode is ≈750 mA h g^{-1} at the second cycle and higher than 800 mA h g^{-1} after 500 cycles.

3. Conclusions

In summary, we have developed an effective spread growth technique for the fabrication of larger-area homogeneous β-$Co(OH)_2$ on graphene with sheet-like and relatively rigid structure. As-prepared hybrid can coat on Cu foil by means of simple layer-by-layer staking. After sintering, as-obtained binder-free electrode as anode of LIBs shows excellent cycling stability from 0 to 55 °C. We also demonstrate as-prepared binder- and conductive carbon-free CoO/graphene hybrid exhibits stable structure even after 5000 charge/discharge cycles. In addition, the large-scale and low-cost fabrication process of binder-free electrode is facile by means of drop-coated method.

4. Experimental Section

Synthesis of Graphene Oxide: Graphene oxide was prepared by a modified Hummers method.[20] graphite powder (0.375 g, Alfa Aesar, AR) and $KMnO_4$ (2.25 g) were added to concentrated H_2SO_4/H_3PO_4 (45:5 mL). After stirring 24 h at 50 °C, the reaction was cooled to room temperature and poured onto ice (200 mL) with H_2O_2 (3 mL, 30%). Then the mixture was centrifuged (12 000 rpm for 5 min). The remaining solid material was washed with of HCl (200 mL, 30%) for twice, and water (200 mL) three times.

Synthesis of Ultrathin Nanosheets of α-Co(OH)$_2$: Ammonia water (1 mL, 25%) was added to $Co(NO_3)_2$ solutions (120 mL, 0.025 M). After stirring for about 5 min, the as-obtained green blue precipitate was washed with deionized water by centrifugation for 3 times at 10 °C, then transferred into a 50 mL of Teflon-lined autoclave, which was filled with solvents (water/methanol, 16 mL/16 mL). And then, these systems were sealed and heated at 180 °C for 30 min.

Synthesis of β-Co(OH)$_2$/Graphene Hybrid: Firstly, graphene oxide solution (10 mL, 9.6 mg of graphene oxide) was added to colloidal solution of α-$Co(OH)_2$ (100 mL, 96 mg of α-$Co(OH)_2$). After the ultrasonic radiation for 30 min, hydrazine monohydrate (0.32 mL) was added to above mixture and refluxed at 95 °C for 24 h. Finally, the resulting β-$Co(OH)_2$/graphene hybrid was subsequently centrifuged, washed with water and dispersed in DMF up to the concentration of 6–8 mg mL^{-1}.

Preparation of Binder-Free Electrode Using Layer-by-Layer Assembled β-Co(OH)$_2$/Graphene: To prepare binder-free electrode, firstly, Cu foil was washed with acetone and dried under vacuum at 80 °C for 3 h. Then, β-$Co(OH)_2$/graphene suspension was dropped on Cu foil and dried at 80 °C for 30 min. The obtained hybrid was deposited on Cu foil by the evaporation of DMF. After pressing under a pressure of 3–5 MPa, the above sample was sintered at 350 °C for 3 h under Ar/H_2 (5% H_2 in volume) atmosphere. The conventional CoO/graphene electrode was prepared by casting slurry containing CoO/graphene hybrid, acetylene black and polyvinylidene fluoride (PVDF) or carboxymethyl cellulose (CMC) at a weight ratio of 8:1:1 on Cu foil.

Material Characterization: XRD measurements were performed on a Rigaku-Dmax 2500 diffractometer with Cu-Kα radiation. SEM was performed on a field emission Hitachi S-4800 instrument. TEM was performed using a FEI Tecnai G_2 S-Twin instrument. XPS analysis was carried on an ESCALAB MK II X-ray photoelectron spectrometer. Zeta potential was measured by dynamic light scattering (Malvern Nano-ZS). Thermogravimetric analysis/differential thermal analysis (TG/DTA) was performed at a heating rate of 2.5 °C min^{-1} in flowing air (NETZSCH STA 449F3, Germany). The porosity was determined by nitrogen sorption using a micrometritics ASAP 2020 analyzer. Raman spectra were collected using a micro-Raman spectrometer (Renishaw) with a laser of 532 nm wavelength. AFM measurements were applied on Bruker Multimode scanning probe microscope with a Nanoscope III A controller in ScanAsyst in Air.

Electrochemical Measurement: The electrochemical experiments were performed via CR2025 coin-type test cells assembled in a dry argon-filled glove box. The test cell consisted of a working electrode and a lithium foil which was separated by a Celgard 2400 membrane. The electrolyte solution was prepared by dissolving 1 M $LiPF_6$ in a 1:1 mass ratio mixture of ethylene carbonate and dimethyl carbonate. Each electrode has approximately 0.3–0.6 mg of active material. Galvanostatic charge-discharge cycling tests were performed using an LAND CT2001A battery testing system in the voltage range between 0.01 V and 3 V. Impedance and the cyclic voltammetry (CV) measurements were performed used a VMP3 Electrochemical workstation (Bio-logic Inc).

Supporting Information

Supporting Information is available from the Wiley Online Library or from the author.

Acknowledgements

This work was financially supported by 100 Talents Programme of The Chinese Academy of Sciences, National Program on Key Basic Research Project of China (973 Program, Grant No. 2012CB215500), National Natural Science Foundation of China (Grant No. 21101147 and 21203176), China Postdoctoral Science Foundation (2011M500624), and Special Foundation of China Postdoctoral Science (2012T50293).

Received: December 20, 2012
Revised: February 3, 2013
Published online: April 9, 2013

[1] a) M. Armand, J. M. Tarascon, *Nature* **2008**, *451*, 652; b) J. B. Goodenough, Y. Kim, *Chem. Mater.* **2010**, *22*, 587; c) B. Kang, G. Ceder, *Nature* **2009**, *458*, 190; d) H. Jung, M. W. Jang, J. Hassoun, Y. Sun, B. Scrosati, *Nat. Commun.* **2011**, *2*, 516; e) Y. Hu, X. Liu, J. Muller, R. Schlogl, J. Maier, D. S. Su, *Angew. Chem. Int. Ed.* **2009**, *48*, 210; f) Z. Song, T. Xu, M. L. Gordin, Y. Jiang, I. Bae, Q. Xiao, H. Zhan, J. Liu, D. Wang, *Nano Lett.* **2012**, *12*, 2205.

[2] a) C. M. Park, J. H. Kim, H. Kim, H. J. Sohn, *Chem. Soc. Rev.* **2010**, *39*, 3115; b) J. Cabana, L. Monconduit, D. Larcher, M. R. Palacin, *Adv. Mater.* **2010**, *22*, E179.

[3] a) P. Poizot, S. Laruelle, S. Grugeon, L. Dupont, J. M. Tarascon, *Nature* **2000**, *407*, 496; b) G. Zhou, D. Wang, L. Yin, N. Li, F. Li, H. Cheng, *ACS Nano* **2012**, *6*, 3214.

[4] I. Kovalenko, B. Zdyrko, A. Magasinski, B. Hertzberg, Z. Milicev, R. Burtovyy, L. I. uzinov, G. Yushin, *Science* **2011**, *334*, 75.

[5] X. Wang, W. Han, H. Chen, J. Bai, T. A. Tyson, X. Yu, X. Wang, X. Yang, *J. Am. Chem. Soc.* **2011**, *133*, 20692.

[6] C. K. Chan, H. Peng, G. Liu, K. Mcilwrath, X. F. Zhang, R. A. Huggins, Y. Cui, *Nat. Nanotechnol.* **2008**, *3*, 31.

[7] H. Zhang, X. Yu, P. V. Braun, *Nat. Nanotechnol.* **2011**, *6*, 277.

[8] X. Xue, S. Yuan, L. Xing, Z. Chen, B. He, Y. Chen, *Chem. Commun.* **2011**, *47*, 4718.

[9] a) H. Wang, L. Cui, Y. Yang, H. Casalongue, J. T. Robinson, Y. Liang, Y. Cui, H. Dai, *J. Am. Chem. Soc.* **2010**, *132*, 13978; b) A. Kushima, X. H. Liu, G. Zhu, Z. L. Wang, J. Y. Huang, J. Li, *Nano Lett.* **2011**, *11*, 4535; c) J. Y. Huang, L. Zhong, C. M. Wang, J. P. Sullivan, W. Xu, L. Q. Zhang, S. X. Mao, N. S. Hudak, X. H. Liu, A. Subramanian, H. Fan, L. Qi, A. Kushima, J. Li, *Science* **2010**, *330*, 1515; d) W. M. Zhang, X. L. Wu, J. S. Hu, Y. G. Guo, L. J. Wan, *Adv. Funct. Mater.* **2008**, *18*, 3941; e) X. H. Lu, T. Zhai, X. H. Zhang, Y. Q. Shen, L. Y. Yuan, B. Hu, L. Gong, J. Chen, Y. Gao, J. Zhou, Y. X. Tong, Z. L. Wang, *Adv. Mater.* **2012**, *24*, 938; f) Y. G. Guo, Y. S. Hu, W. Sigle, J. Maier, *Adv. Mater.* **2007**, *19*, 2087.

[10] a) L. Zhang, L. Jiang, H. Yan, W. D. Wang, W. Wang, W. Song, Y. Guo, L. Wan, *J. Mater. Chem.* **2010**, *20*, 5462; b) M. Zhang, D. Lei, Z. Du, X. Yin, L. Chen, Q. Li, Y. Wang, T. Wang, *J. Mater. Chem.* **2011**, *21*, 1673; c) J. Zhu, T. Zhu, X. Zhou, Y. Zhang, X. W. Lou, X. Chen, H. Zhang, H. H. Hng, Q. Yan, *Nanoscale* **2011**, *3*, 1084.

[11] a) S. Ding, D. Luan, F. Y. C. Boey, J. S. Chen, X. W. Lou, *Chem. Commun.* **2011**, *47*, 7155; b) L. Q. Lu, Y. Wang, *J. Mater. Chem.* **2011**, *21*, 17916; c) Y. Huang, X. Huang, J. Lian, D. Xu, L. Wang, X. Zhang, *J. Mater. Chem.* **2012**, *22*, 2844.

[12] a) Z. Chen, M. Zhou, Y. Cao, X. Ai, H. Yang, J. Liu, *Adv. Energy Mater.* **2011**, *2*, 95; b) Y. Sun, X. Hu, W. Luo, Y. Huang, *J. Mater. Chem.* **2012**, *22*, 425.

[13] Z. Liu, R. Ma, M. Osada, K. Takada, T. Sasaki, *J. Am. Chem. Soc.* **2005**, *127*, 13869.

[14] a) X. Huang, X. Qi, F. Boey, H. Zhang, *Chem. Soc. Rev.* **2012**, *41*, 666; b) Y. Zhu, S. Murali, W. Cai, X. Li, J. W. Suk, J. R. Potts, R. S. Ruoff, *Adv. Mater.* **2010**, *22*, 3906; c) Z. Fan, W. Kai, J. Yan,

T. Wei, L. Zhi, J. Feng, Y. Ren, L. Song, F. Wei, *ACS Nano* **2011**, *5*, 191; d) L. Zhang, J. Liang, Y. Huang, Y. Ma, Y. Wang, Y. Chen, *Carbon* **2009**, *47*, 3365.

[15] a) S. Stankovich, D. A. Dikin, R. D. Piner, K. A. Kohlhaas, A. Kleinhammes, Y. Jia, Y. Wu, S. T. Nguyen, R. S. Ruoff, *Carbon* **2007**, *45*, 1558; b) J. Chen, K. Sheng, P. Luo, C. Li, G. Shi, *Adv. Mater.* **2012**, *24*, 4569; c) I. K. Moon, J. Lee, R. S. Ruoff, H. Lee, *Nat. Commun.* **2010**, *1*, 73.

[16] a) S. Brutti, V. Gentili, H. Menard, B. Scrosati, P. G. Bruce, *Adv. Energy Mater.* **2012**, *2*, 322; b) C. Peng, B. Chen, Y. Qin, S. Yang, C. Li, Y. Zuo, S. Liu, J. Yang, *ACS Nano* **2012**, *6*, 1074.

[17] a) P. R. Abel, Y. M. Lin, H. Celio, A. Heller, C. B. Mullins, *ACS Nano* **2012**, *6*, 2506; b) Y. Li, B. Tan, Y. Wu, *Nano lett.* **2008**, *8*, 265.

[18] L. Chen, X. Xie, J. Xie, K. Wang, J. Yang, *J. Appl. Electrochem.* **2006**, *36*, 1099.

[19] a) C. K. Huang, J. S. Sakamoto, J. Wolfenstine, S. Surampudi, *J. Electrochem. Soc.* **2000**, *147*, 2893; b) J. Yan, A. Sumboja, E. Khoo, P. S. Lee, *Adv. Mater.* **2011**, *23*, 746.

[20] D. C. Marcano, D. V. Kosynkin, J. M. Berlin, A. Sinitskii, Z. Sun, A. Slesarev, L. B. Alemany, W. Lu, J. M. Tour, *ACS Nano* **2010**, *4*, 4806.